

Nanozyme Based on Porphyrinic Metal–Organic Framework for Electrocatalytic CO₂ Reduction

Junghye Lee, Hansaem Choi, Jinhong Mun, Eunji Jin, Soochan Lee, Joochan Nam, Muhammad Umer, Jaeheung Cho, Geunsik Lee,* Youngkook Kwon,* and Wonyoung Choe*

Mimicry of natural enzyme systems is an important approach for catalyst design. To create an enzyme-inspired catalyst, it is essential to mimic both the active center and the second coordination sphere. Metal–organic frameworks (MOFs), an emerging class of porous materials, are ideal candidates for heterogeneous catalysts because their versatile building blocks confer a high level of structural tunability, and the chemical environment surrounding the active center can be controlled at the molecular level. Herein, a new 2D porphyrinic MOF, PPF-100, constructed from a nonplanar saddle-distorted porphyrin linker and a Cu paddle-wheel metal node is reported. The strategic introduction of ethyl substituents allows not only to mimic the active center and second coordination sphere but also to increase the catalytic selectivity while completely inhibiting H₂ generation in the CO₂ reduction reaction.

1. Introduction

Natural enzymes are molecular machines capable of catalyzing countless substrates to produce essential products for living creatures.^[1] Mimicking their extraordinary catalytic capabilities has been an objective in numerous disciplines, including the energy sciences.^[2–5] Two important approaches have been developed to create catalytically active artificial enzyme mimics. They are: 1) to build homogeneous or heterogeneous catalysts whose

structures mimic the active centers of natural enzymes;^[6–13] and 2) to tune the second coordination sphere, by adjusting properties such as hydrophobicity, hydrogen bonding, and ionic interactions around active centers, to be similar to those found in nature.^[14–21] Although the former approach has been extensively studied over the past few decades, the latter is becoming popular as an approach to drastically enhance catalytic performance through the introduction of substituents and hydrophobicity control, as exemplified by the O₂ reduction reaction (ORR)^[22,23] and the CO₂ reduction reaction (CO₂RR).^[24–27]

The importance of the second coordination sphere has been also highlighted through research on the zinc-containing enzyme, carbonic anhydrase, which catalyzes the reversible hydration of CO₂ and dehydration of HCO₃[−]; it was suggested that the hydrophobic region at the active center is responsible for CO₂ binding, which increases the catalytic activity.^[28] Similar hydrophobic microenvironments are also found in heme-containing enzymes. For example, cytochrome *c* peroxidase has hydrophobic substrate residues located adjacent to the heme active center (Scheme 1).^[29]


We combined these two useful characteristics, active centers and tunable second coordination spheres, in one compound using metal–organic frameworks (MOFs), an emerging class of porous materials, aiming for electrocatalytic CO₂RR application.^[30–33] MOFs are a versatile material platform because the building blocks are highly modifiable, from organic linkers to metal nodes, providing virtually limitless choices.^[34] Prime examples are porphyrinic MOFs that target artificial heme enzyme function.^[35,36] Most porphyrin-based MOFs are constructed with simple planar porphyrin linkers.^[37–41] Zhou et al. reported that MOFs with substituted porphyrin linkers around porphyrin active centers could significantly alter catalytic activity, selectivity, and stability. However, the role of the second coordination sphere was not clearly demonstrated.^[42] In this regard, we envisioned that a porphyrinic MOF with a highly substituted porphyrin linker could tune the second coordination sphere around the catalytic centers, as well as the electronic structure of porphyrin.^[43–46]

Here, we report a new bio-inspired 2D porphyrinic MOF, PPF-100 (PPF stands for Porphyrinic Paddle-wheel Framework), constructed from a nonplanar porphyrin linker

J. Lee, J. Mun, E. Jin, S. Lee, J. Nam, M. Umer, J. Cho, G. Lee, W. Choe
Department of Chemistry
Ulsan National Institute of Science and Technology (UNIST)
Ulsan 44919, Republic of Korea
E-mail: gslee@unist.ac.kr; choe@unist.ac.kr

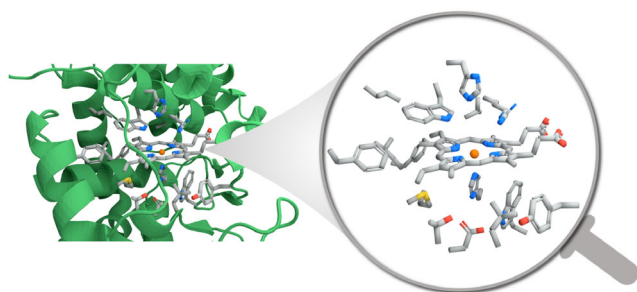
H. Choi, Y. Kwon
School of Energy and Chemical Engineering
Ulsan National Institute of Science of Technology (UNIST)
Ulsan 44919, Republic of Korea
E-mail: ykwon@unist.ac.kr

Y. Kwon, W. Choe
Graduate School of Carbon Neutrality
Ulsan National Institute of Science and Technology (UNIST)
Ulsan 44919, Republic of Korea

 The ORCID identification number(s) for the author(s) of this article can be found under <https://doi.org/10.1002/ssstr.202200087>.

© 2022 The Authors. Small Structures published by Wiley-VCH GmbH. This is an open access article under the terms of the Creative Commons Attribution License, which permits use, distribution and reproduction in any medium, provided the original work is properly cited.

DOI: 10.1002/ssstr.202200087



Scheme 1. The crystal structure of cytochrome *c* peroxidase (PDB ID: 4A6Z). Heme active center and surrounding residues.

and a Cu paddle-wheel node. By substituting an ethyl group at the β -position of the porphyrin linker, it is possible to have nonplanar saddle-distorted macrocycle conformation and create hydrophobicity at the same time. The porphyrin distortion causes cavities on both sides of the macrocycle, resulting in discrete cavities within the PPF-100 structure. PPF-100 exhibits exceptional hydrophobicity and remarkable water and chemical stability. PPF-100 nanozyme was also synthesized via a surfactant-mediated synthetic procedure. PPF-100

nanozyme displayed significantly enhanced selectivity for CO₂RR and completely suppressed the hydrogen evolution reaction (HER).

2. Results and Discussion

2.1. Synthesis and Characterization of Bulk PPF-100 Crystals

PPF-100 crystals were synthesized with Cu(NO₃)₂·2.5H₂O and OETPP (2,3,7,8,12,13,17,18-(octaethyl)-5,10,15,20-tetrakis(4-carboxybiphenyl)porphyrin) as a linker via a solvothermal reaction. Single-crystal X-ray diffraction analysis showed that PPF-100 crystallizes in the form of the tetragonal space group of *I*₄₁/*amd* (Table S1, Supporting Information). As shown in **Figure 1a**, PPF-100 is composed of Cu paddle-wheels, Cu₂(COO)₄, and OETPP linkers. During the reaction, the OETPP linker was metallated in situ and connected by Cu paddle-wheel clusters to form a 2D square grid layer (**Figure 1b**). These grids were stacked in an ABCD packing pattern and the interlayer distance according to the unit cell parameter was 4.7 Å (**Figure 1c**). In this arrangement, the Cu center of the porphyrin linker was arranged vertically with the paddle-wheel Cu atom, where the *N*, *N'*-dimethylformamide (DMF) molecules are coordinated to the

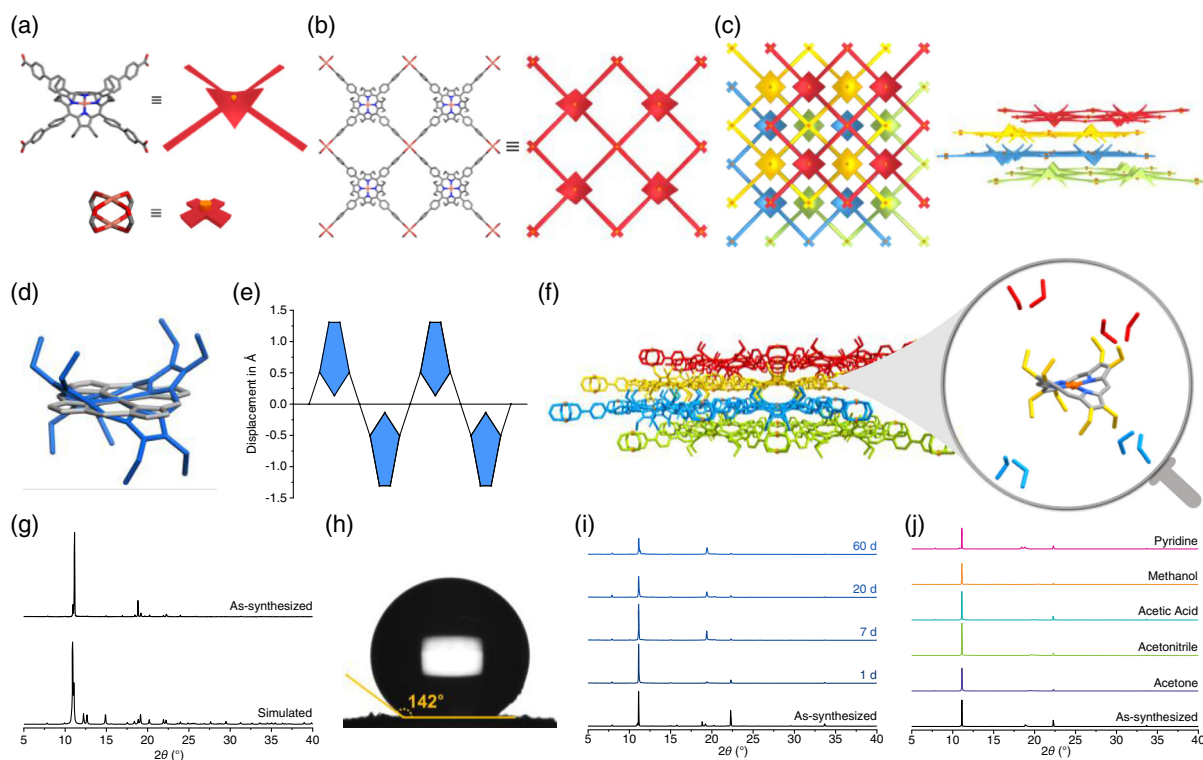


Figure 1. Description of the PPF-100 structure. a) OETPP linker (top) and Cu paddle-wheel (bottom). A red square of the OETPP linker shows saddle distortion. An orange button represents the Cu metal. b) The single-layer structure of PPF-100. c) The stacking pattern of PPF-100; top (left) and side view (right). d) Illustration of planar porphyrin (gray) and OETPP linker macrocycles (blue). e) The degree of nonplanarity in porphyrin is determined by the skeletal deviation plot of OETPP linker macrocycle atoms. The deviations from the mean plane are composed of 24 ring atoms. f) In the stacked layers of PPF-100, the ethyl groups are located around the OETPP macrocycle. g) Simulated and experimental powder X-ray diffraction patterns of bulk PPF-100. h) Contact angle image of bulk PPF-100. i) PXRD patterns of as-synthesized PPF-100 crystals before and after being immersed in water for 60 days at ambient temperature. j) PXRD patterns of PPF-100 crystals after exposure to different organic solvents for 1 week (purple; acetone, green; acetonitrile, bluish green; acetic acid, orange; methanol, pink; pyridine).

Cu paddle-wheels. The distance between the porphyrin Cu atom and the paddle-wheel Cu atom was 8.1 Å.

Most porphyrin-based MOFs are based on planar porphyrin linkers. Porphyrin linkers typically vary in length and functional group at the *meso*-position of the porphyrin ring. Interestingly, nonplanar tetrapyrrole porphyrins have been observed in several protein complexes. Among nonplanar porphyrins, commonly observed types include saddle, ruffle, dome, wavy, and propeller types.^[47] In PPF-100, the OETPP linker shows a highly nonplanar saddle macrocycle conformation due to the steric crowding of the peripheral substituents and β -pyrrole ethyl groups. To compare the conformation of porphyrin, the planar- and saddle-distorted porphyrin rings were overlapped. Figure 1d shows the macrocycle of the OETPP linker (blue) and the planar porphyrin (gray). The skeletal deviation plot represents the degree of out-of-plane distortion, showing the highly nonplanar nature of the porphyrin macrocycle of the OETPP linker (Figure 1e). OETPP linker shows a displacement of the β -pyrrole position of 1.3 Å out of the mean plane defined by the 24 atoms of the macrocycle, and its saddle geometry is characterized by an alternating displacement of the pyrrole units above and below the mean plane. In the stacked layers of PPF-100, the ethyl groups of the OETPP linker are adjacent to the porphyrin metal center (Figure 1f). The corresponding distances between porphyrin Cu metal and ethyl substitutions are 5.6 and 11.3 Å (Figure S1, Supporting Information). The experimental powder X-ray diffraction (PXRD) pattern of PPF-100 corresponds to the simulated pattern obtained from the single-crystal data (Figure 1g). The gas adsorption performance of PPF-100 was evaluated for N₂ and CO₂. Two distinct steps were observed in the N₂ adsorption isotherm at 77 K (Figure S2, Supporting Information). A large degree of hysteresis appeared, and high uptake was maintained at very low pressure. The Brunauer–Emmett–Teller (BET) surface area was 398.3 m² g⁻¹ (Figure S3, Supporting Information). The pore size distribution (PSD) exhibits microporosity based on the N₂ adsorption isotherm (Figure S4, Supporting Information). The CO₂ isotherms of PPF-100, acquired at 195, 273, and 293 K, indicated moderate CO₂ uptakes of 8.8, 3.3, and 2.6 mmol g⁻¹ at 1 bar, respectively (Figure S5, Supporting Information). The isosteric heat of adsorption (Q_{st}) calculated by fitting the CO₂ isotherms to the single-site Langmuir–Freundlich equation indicated an initial Q_{st} value of -31.7 kJ mol⁻¹ (Figure S6, Supporting Information). The solvent content of the activated PPF-100 was confirmed through the ¹H NMR and thermogravimetric analysis (Figure S7 and S8, Supporting Information). In the framework, approximately 7.5 DMF molecules are contained in the unit cell of PPF-100. The hydrophobicity of PPF-100 was determined by evaluating the water contact angle. The external surface of MOFs is generally described as superhydrophobic if the water contact angle is greater than 150°. ^[48,49] Surprisingly, the water contact angle measured on bulk PPF-100 crystals was 142°, indicating near superhydrophobic as shown in Figure 1h. In addition, to test the water stability of PPF-100, PXRD was performed on a sample soaked in deionized water for 2 months. As shown in Figure 1i, the PXRD patterns of the water-soaked samples show reflections corresponding to that of the as-synthesized sample, confirming that the structure of PPF-100 was well maintained in water. After 2 months of soaking in water, the PXRD pattern of PPF-100 did not show any major

changes. This is attributed to the hydrophobic ethyl functional groups of the OETPP linker around the Cu paddle-wheel that effectively protects the metal node from attack by water. To investigate the chemical stability of PPF-100, freshly prepared PPF-100 crystals were soaked in various organic solvents for 1 week, including acetone, acetonitrile, acetic acid, methanol, and pyridine. PPF-100 demonstrated remarkable chemical stability in various organic solvents (Figure 1j). Among 2D MOFs consisting of Cu metal nodes, these hydrophobicity and chemical stability characteristics are exceptionally rare.

2.2. Investigation of PPF-100 Nanozyme

MOF nanosheets are significantly important for fundamental structural research and technological developments due to their unique properties originating from the ultrathin thickness and large surface area with highly active sites.^[50–52] The PPF-100 nanozyme was prepared by a bottom-up synthesis method.^[53] Polyvinylpyrrolidone was used as the surfactant to control the size and shape of the nanocrystals via the selective attachment on the MOF surfaces. The crystallinity of the PPF-100 nanozyme was examined by synchrotron PXRD. The PXRD pattern of the PPF-100 nanozyme was consistent with that of the bulk PPF-100 crystal, indicating that the PPF-100 nanozyme structure is identical to that of the bulk PPF-100 structure (Figure 2a). The SEM image of the PPF-100 nanozyme is uniformly synthesized in a disk-like morphology (Figure S9, Supporting Information). The Tyndall effect was observed when ethanol was used as a solvent for the PPF-100 nanozyme which confirms their colloidal structure (Figure S10, Supporting Information). The AFM image and height profiles of PPF-100 nanozyme were obtained (Figure 2b,c). It is analyzed that the average thickness and lateral size of PPF-100 nanozyme are 45 and 822 nm, respectively (Figure S11, Supporting Information). The water contact angle measured on PPF-100 nanozyme was also 142°, the same result as bulk PPF-100 crystals (Figure 2d). The TEM image shows the morphology of PPF-100 nanozyme clearly (Figure 2e). Also, lattice fringes were observed, corresponding to (220) plane, where d value is 1.06 nm (Figure 2f). According to the fast Fourier transform (FFT) image, (220) and ($\bar{2}\bar{2}0$) planes were detected which means the orientation of the PPF-100 nanozyme is along [001] zone axis (Figure S12, Supporting Information). For clarity, Fourier filter and low-pass filter were applied to Figure 2f resulting in Figure 2g, which is in perfect agreement with the PPF-100 structure. The N₂ isotherm of the PPF-100 nanozyme was also obtained by N₂ sorption analysis at 77 K (Figure S13, Supporting Information). The PPF-100 nanozyme exhibits a specific BET surface area of 585.6 m² g⁻¹, and is higher than the bulk PPF-100 crystals (Figure S14, Supporting Information).

The PSD data of PPF-100 nanozyme obtained from the N₂ adsorption isotherm show the identical microporosity as bulk PPF-100 (Figure S15, Supporting Information). The CO₂ isotherms of the PPF-100 nanozyme were obtained at 273 and 293 K and indicated moderate CO₂ uptake of 2.8 and 2.3 mmol g⁻¹ at 1 bar, respectively (Figure S16, Supporting Information). We also confirmed the chemical stability of PPF-100 nanozyme. The freshly prepared PPF-100 nanozyme samples were soaked in various organic solvents

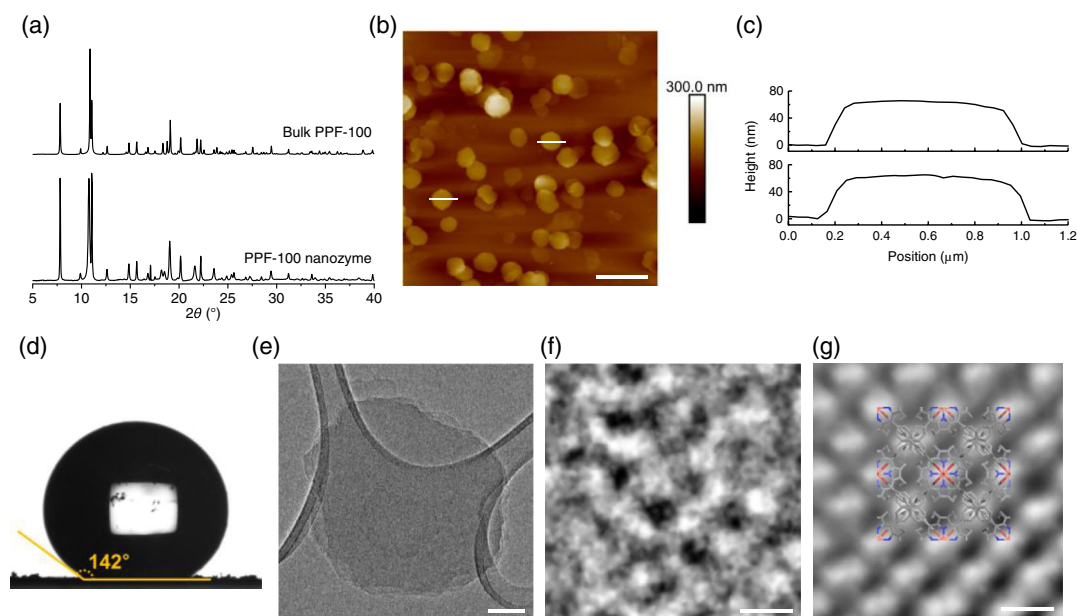


Figure 2. a) Synchrotron powder X-ray diffraction patterns of bulk PPF-100 crystals and nanozyme. b) AFM image (scale bar, 2 μm) of PPF-100 nanozyme with c) corresponding height profiles. d) Contact angle image of PPF-100 nanozyme. e) TEM image (scale bar, 100 nm) and f) enlarged TEM image (scale bar, 1 nm) of PPF-100 nanozyme viewing down the [001] zone axis. g) Fourier and low-pass filtered version of the TEM image, with the PPF-100 structure, overlaid.

(acetone, acetonitrile, acetic acid, methanol, and pyridine) for 1 week. The PPF-100 nanozyme exhibits significant chemical stability judging from PXRD patterns (Figure S17, Supporting Information).

2.3. Electrocatalytic CO_2 Reduction

Recently, porphyrin-based 2D MOFs have been suggested for use as CO_2 reduction catalysts, owing to their highly exposed and well-defined catalytic active sites.^[38–40] Most of the porphyrin-based 2D MOFs used as CO_2 reduction catalysts are composed of planar porphyrin linkers. However, nonplanar-distorted porphyrin-based 2D MOFs have not been tested. Nonplanar porphyrins substituted with functional groups can provide outstanding hydrophobicity, increase in catalytic activity,^[45] and tunable axial binding strengths.^[54,55]

One major factor in the loss of catalytic efficiency in CO_2 reduction is the competition with the hydrogen evolution reactions (HER). These reactions are commonly performed in an aqueous electrolyte, and H_2 generation is virtually unavoidable.^[56] The hydrophobic surface of the materials can play a key role in increasing the catalytic selectivity in the CO_2 reduction reaction by inhibiting H_2 generation. Similarly, Mougel et al. reported a hydrophobic Cu dendrite that significantly reduced H_2 evolution, which led to an increase in CO_2 reduction selectivity.^[25] We envisioned that such hydrophobicity could enhance CO_2 reduction in 2D porphyrinic MOFs. We conducted the electrocatalytic conversion of CO_2 (CO_2RR) using PPF-100 nanozyme. The CO_2RR activity of PPF-100 nanozyme was evaluated in CO_2 saturated dimethylsulfoxide (DMSO) solvent in the presence of 0.5 M 1-butyl-3-methylimidazolium tetrafluoroborate (BMImBF_4) and 1 M distilled water.^[57,58] The linear

sweep voltammograms (LSV) after *iR*-correction based on impedance spectroscopy (Figure S18, Supporting Information) were recorded in Ar and CO_2 -saturated electrolytes from 0 to -3.0 V versus Ag/Ag^+ (Figure 3a). Compared to the LSV curves in the Ar-saturated electrolyte, a higher current density is observed for PPF-100 nanozyme in the CO_2 -saturated electrolyte, indicating the possible catalytic activity of the PPF-100 nanozyme for electrochemically reducing CO_2 . Online product analyses using gas- and liquid-chromatography were performed^[59] during chronoamperometric electrolysis (Figure S19, Supporting Information). The two predominant products were CO and HCOOH, and a trace amount of CH_4 was detected. We note that the PPF-100 nanozyme had no H_2 evolution activity, compared to other porphyrin-based 2D MOF, $\text{Cu}_2(\text{CuTCPP})$, which generated a nonnegligible amount of H_2 .^[39] This indicates that the hydrophobic PPF-100 is regarded to play a significant role in the suppression of HER. The highest Faradaic efficiencies (FE) for CO and HCOOH were recorded as 72.4 and 24.1, respectively at -3.0 V versus Ag/Ag^+ (Figure 3b). Furthermore, the partial current density of CO of PPF-100 nanozyme reached 2.33 mA cm^{-2} at -3.0 V versus Ag/Ag^+ (Figure 3c). Given that selectively reducing CO_2 to CO as a predominant gaseous product is a promising process as CO is an important feedstock chemical for the generation of other carbon products and to formate as a sole liquid product, PPF-100 nanozyme shows significant catalytic performance for electrochemical conversion with complete suppression of H_2 . Furthermore, the structural stability of PPF-100 nanozyme before and after electrocatalysis was investigated. PXRD peaks are maintained as shown in Figure S20, Supporting Information, indicating that there is no significant structural change after the electrocatalytic CO_2 reduction reaction.

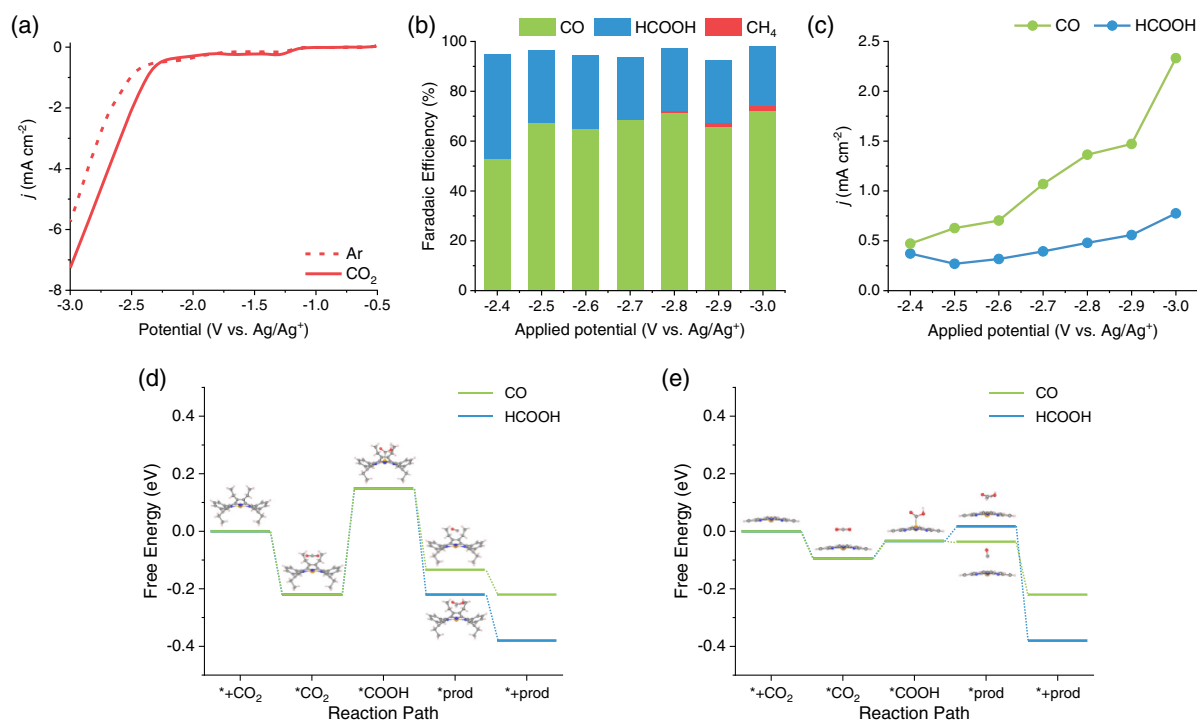


Figure 3. Electrochemical characteristics of PPF-100 nanozyme for CO₂ reduction reaction. a) Linear sweep voltammetry curves for PPF-100 nanozyme in Ar- and CO₂-saturated 0.5 M BMImBF₄ + H₂O/DMSO, b) product distributions at applied potentials, c) partial current densities for CO and HCOOH. Free energy diagrams of CO₂ reduction to CO (green) and HCOOH (blue) for molecular moiety of d) OETPP, and e) TCPP.

To understand the CO₂ reduction reaction activity of PPF-100 nanozyme, we calculated the Gibbs free energies using the density functional theory (DFT) method. Two geometries have been compared, molecular moiety of OETPP and tetra (4-carboxyphenyl)porphyrin (TCPP), as shown in Figure 3d,e. In the case of TCPP, both CO₂ and CO molecules adsorb on Cu metal site weakly with $\Delta G_{*CO_2} = -0.09$ eV and $\Delta G_{*CO} = -0.04$ eV, respectively (Figure 3e). In contrast, OETPP binds more strongly to CO₂ and CO with $\Delta G_{*CO_2} = -0.22$ eV and $\Delta G_{*CO} = -0.13$ eV (Figure 3d). This enhancement originates from attractive interaction between intermediates and ethyl group in PPF-100. Also, enhanced CO adsorption by ethyl groups in PPF-100 nanozyme helps the reaction proceed further toward CH₄ production.

3. Conclusion

In summary, a 2D porphyrinic MOF, PPF-100, was successfully synthesized using a Cu paddle-wheel and a nonplanar saddle-distorted porphyrin linker with an ethyl group substituted at the β -position. Moreover, PPF-100 exhibited hydrophobicity and remarkable water and chemical stability. PPF-100 nanozyme was successfully prepared and found to be suitable for application as CO₂ reduction catalysts. Furthermore, the PPF-100 nanozyme exhibited significant catalytic performance for the electrochemical conversion of CO₂ to CO. Based on our experimental results and DFT calculations, the catalytic selectivity can be attributed to the interaction between intermediates and ethyl groups. We present our efforts to develop a new design strategy

that mimics the active center and tunes the secondary coordination sphere are improved to both highly effective CO₂ catalyst systems. We expect this strategy to be utilized not only in PPF-100 but also in numerous other MOFs in the future.

Supporting Information

Supporting Information is available from the Wiley Online Library or from the author.

Acknowledgements

J.L. and H.C. contributed equally to this work. This work was supported by the National Research Foundation (NRF) of Korea (NRF-2016R1A5A1009405, NRF-2020R1A2C3008226, NRF-2021M3I3A1084909, NRF-2020M3H7A1098231, and NRF-2021R1A2C1006039), the Korea Environment Industry & Technology Institute (KEITI) through Public Technology Program based on Environmental Policy Program, funded by the Korea Ministry of Environment (MOE) (2018000210002) and the Carbon Neutral Institute Research Fund (Project # 1.220099.01) of Ulsan National Institute of Science & Technology (UNIST). The authors acknowledge the Pohang Accelerator Laboratory (PAL) for 6D beamline use (2019-2nd-6D-A025, 2020-1st-6D-A001). This study contains the results obtained by using the equipment of UNIST Central Research Facilities (UCRF).

Conflict of Interest

The authors declare no conflict of interest.

Data Availability Statement

The data that supports the findings of this study are available in the supplementary material of this article. CCDC 2004846 contains the supplementary crystallographic data for this paper. These data can be obtained free of charge from the Cambridge Crystallographic Data Centre via https://www.ccdc.cam.ac.uk/data_request/cif.

Keywords

CO₂ reduction reactions, hydrophobicity, metal–organic frameworks, nanosheets, nanozymes, porphyrin

Received: April 28, 2022

Revised: September 20, 2022

Published online:

- [1] T. L. Poulos, *Chem. Rev.* **2014**, *114*, 3919.
- [2] R. B. Leveson-Gower, C. Mayer, G. Roelfes, *Nat. Rev. Chem.* **2019**, *3*, 687.
- [3] K. Chen, F. H. Arnold, *Nat. Catal.* **2020**, *3*, 203.
- [4] S.-M. Jung, J. Lee, W. J. Song, *J. Inorg. Biochem.* **2021**, *223*, 111552.
- [5] P. Trogadas, M.-O. Coppens, *Chem. Soc. Rev.* **2020**, *49*, 3107.
- [6] S. Ji, B. Jiang, H. Hao, Y. Chen, J. Dong, Y. Mao, Z. Zhang, R. Gao, W. Chen, R. Zhang, Q. Liang, H. Li, S. Liu, Y. Wang, Q. Zhang, L. Gu, D. Duan, M. Liang, D. Wang, X. Yan, Y. Li, *Nat. Catal.* **2021**, *4*, 407.
- [7] F. Franco, C. Rettenmaier, H. S. Jeon, B. R. Cuenya, *Chem. Soc. Rev.* **2020**, *49*, 6884.
- [8] L. Huang, J. Chen, L. Gan, J. Wang, S. Dong, *Sci. Adv.* **2019**, *5*, eaav5490.
- [9] L. Xie, X.-P. Zhang, B. Zhao, P. Li, J. Qi, X. Guo, B. Wang, H. Lei, W. Zhang, U.-P. Apfel, R. Cao, *Angew. Chem., Int. Ed.* **2021**, *60*, 7576.
- [10] Z. Weng, Y. Wu, M. Wang, J. Jiang, K. Yang, S. Huo, X.-F. Wang, Q. Ma, G. W. Brudvig, V. S. Batista, Y. Liang, Z. Feng, H. Wang, *Nat. Commun.* **2018**, *9*, 415.
- [11] P. Mondal, G. B. Wijeratne, *J. Am. Chem. Soc.* **2020**, *142*, 1846.
- [12] T. Hayashi, M. Tinzl, T. Mori, U. Krenkel, J. Proppe, J. Soetbeer, D. Klose, G. Jeschke, M. Reiher, D. Hilvert, *Nat. Catal.* **2018**, *1*, 578.
- [13] N. G. Yasri, T. A. Al-Attas, J. Hu, M. G. Kibria, *Catal. Sci. Technol.* **2021**, *11*, 1580.
- [14] C. Long, K. Wan, X. Qiu, X. Zhang, J. Han, P. An, Z. Yang, X. Li, J. Guo, X. Shi, H. Wang, Z. Tang, S. Liu, *Nano Res.* **2022**, *15*, 1817.
- [15] J. Li, Y. Zhang, N. Kornienko, *New J. Chem.* **2020**, *44*, 4246.
- [16] J. C. Lewis, *ACS Catal.* **2013**, *3*, 2954.
- [17] F. Nastri, D. D'Alonzo, L. Leone, G. Zambrano, V. Pavone, A. Lombardi, *Trends Biochem. Sci.* **2019**, *44*, 1022.
- [18] K. Oohora, A. Onoda, T. Hayashi, *Acc. Chem. Res.* **2019**, *52*, 945.
- [19] L. Villarino, K. E. Splan, E. Reddem, L. Alonso-Cotchico, C. Gutiérrez de Souza, A. Lledós, J.-D. Maréchal, A.-M. W. H. Thunnissen, G. Roelfes, *Angew. Chem., Int. Ed.* **2018**, *57*, 7785.
- [20] M. Vonesch, J. A. Wytko, H. Kitagishi, K. Kano, J. Weiss, *Chem. Commun.* **2019**, *55*, 14558.
- [21] S. Fukuzumi, Y.-M. Lee, H. S. Ahn, W. Nam, *Chem. Sci.* **2018**, *9*, 6017.
- [22] S. Dey, B. Mondal, S. Chatterjee, A. Rana, S. Amanullah, A. Dey, *Nat. Rev. Chem.* **2017**, *1*, 0098.
- [23] B. Lv, X. Li, K. Guo, J. Ma, Y. Wang, H. Lei, F. Wang, X. Jin, Q. Zhang, W. Zhang, R. Long, Y. Xiong, U.-P. Apfel, R. Cao, *Angew. Chem., Int. Ed.* **2021**, *60*, 12742.
- [24] Z.-Z. Niu, F.-Y. Gao, X.-L. Zhang, P.-P. Yang, R. Liu, L.-P. Chi, Z.-Z. Wu, S. Qin, X. Yu, M.-R. Gao, *J. Am. Chem. Soc.* **2021**, *143*, 8011.
- [25] D. Wakerley, S. Lamaison, F. Ozanam, N. Menguy, D. Mercier, P. Marcus, M. Fontecave, V. Mougel, *Nat. Mater.* **2019**, *18*, 1222.
- [26] Z. Xing, L. Hu, D. S. Ripatti, X. Hu, X. Feng, *Nat. Commun.* **2021**, *12*, 136.
- [27] H.-Q. Liang, S. Zhao, X.-M. Hu, M. Ceccato, T. Skrydstrup, K. Daasbjerg, *ACS Catal.* **2021**, *11*, 958.
- [28] J. K. Kim, C. Lee, S. W. Lim, A. Adhikari, J. T. Andring, R. McKenna, C.-M. Ghim, C. U. Kim, *Nat. Commun.* **2020**, *11*, 4557.
- [29] I. Bertini, S. Chevance, R. Del Conte, D. Lalli, P. Turano, *PLoS One* **2011**, *6*, 18329.
- [30] K. Chen, X.-L. Wang, W. Hu, Q. Kong, H. Pang, Q. Xu, *Small Struct.* **2022**, *3*, 2100200.
- [31] S. S. A. Shah, T. Najam, M. Wen, S.-Q. Zang, A. Waseem, H.-L. Jiang, *Small Struct.* **2022**, *3*, 2100090.
- [32] C. S. Diercks, Y. Liu, K. E. Cordova, O. M. Yaghi, *Nat. Mater.* **2018**, *17*, 301.
- [33] M. K. Lee, M. Shokouhimehr, S. Y. Kim, H. W. Jang, *Adv. Energy Mater.* **2022**, *12*, 2003990.
- [34] M. J. Kalmutzki, N. Hanikel, O. M. Yaghi, *Sci. Adv.* **2018**, *4*, eaat9180.
- [35] J. Chen, Y. Zhu, S. Kaskel, *Angew. Chem., Int. Ed.* **2021**, *60*, 5010.
- [36] L. Feng, K.-Y. Wang, E. Joseph, H.-C. Zhou, *Trends Chem.* **2020**, *2*, 555.
- [37] Z. Liang, H.-Y. Wang, H. Zheng, W. Zhang, R. Cao, *Chem. Soc. Rev.* **2021**, *50*, 2540.
- [38] D. Yang, S. Zuo, H. Yang, Y. Zhou, X. Wang, *Angew. Chem., Int. Ed.* **2020**, *59*, 18954.
- [39] J.-X. Wu, S.-Z. Hou, X.-D. Zhang, M. Xu, H.-F. Yang, P.-S. Cao, Z.-Y. Gu, *Chem. Sci.* **2019**, *10*, 2199.
- [40] Y. Zhou, S. Chen, S. Xi, Z. Wang, P. Deng, F. Yang, Y. Han, Y. Pang, B. Y. Xia, *Cell Rep. Phys. Sci.* **2020**, *1*, 100182.
- [41] C. Wang, C.-Y. Zhu, M. Zhang, Y. Geng, Y.-G. Li, Z.-M. Su, *J. Mater. Chem. A* **2020**, *8*, 14807.
- [42] N. Huang, S. Yuan, H. Drake, X. Yang, J. Pang, J. Qin, J. Li, Y. Zhang, Q. Wang, D. Jiang, H.-C. Zhou, *J. Am. Chem. Soc.* **2017**, *139*, 18590.
- [43] M. Kielmann, M. O. Senge, *Angew. Chem., Int. Ed.* **2019**, *58*, 418.
- [44] K. Norvaiša, K. J. Flanagan, D. Gibbons, M. O. Senge, *Angew. Chem., Int. Ed.* **2019**, *58*, 16553.
- [45] M. Kielmann, N. Grover, W. W. Kalisch, M. O. Senge, *Eur. J. Org. Chem.* **2019**, *2019*, 2448.
- [46] M. Roucan, M. Kielmann, S. J. Connon, S. S. R. Bernhard, M. O. Senge, *Chem. Commun.* **2018**, *54*, 26.
- [47] M. O. Senge, S. A. MacGowan, J. M. O'Brien, *Chem. Commun.* **2015**, *51*, 17031.
- [48] K. Jayaramulu, F. Geyer, A. Schneemann, Š. Kment, M. Otyepka, R. Zboril, D. Vollmer, R. A. Fischer, *Adv. Mater.* **2019**, *31*, 1900820.
- [49] S. Mukherjee, S. Sharma, S. K. Ghosh, *APL Mater.* **2019**, *7*, 050701.
- [50] S. Dang, Q.-L. Zhu, Q. Xu, *Nat. Rev. Mater.* **2017**, *3*, 17075.
- [51] M. Zhao, Y. Huang, Y. Peng, Z. Huang, Q. Ma, H. Zhang, *Chem. Soc. Rev.* **2018**, *47*, 6267.
- [52] D. J. Ashworth, J. A. Foster, *J. Mater. Chem. A* **2018**, *6*, 16292.
- [53] Y. Wang, M. Zhao, J. Ping, B. Chen, X. Cao, Y. Huang, C. Tan, Q. Ma, S. Wu, Y. Yu, Q. Lu, J. Chen, W. Zhao, Y. Ying, H. Zhang, *Adv. Mater.* **2016**, *28*, 4149.
- [54] T. Kojima, T. Nakanishi, T. Honda, R. Harada, M. Shiro, S. Fukuzumi, *Eur. J. Inorg. Chem.* **2009**, *2009*, 727.
- [55] T. Ishizuka, S. Fukuzumi, T. Kojima, *J. Porphyrins Phthalocyanines* **2015**, *19*, 32.
- [56] A. Goyal, G. Marcandalli, V. A. Mints, M. T. M. Koper, *J. Am. Chem. Soc.* **2020**, *142*, 4154.
- [57] M. König, J. Vaes, E. Klemm, D. Pant, *iScience* **2019**, *19*, 135.
- [58] H.-K. Lim, Y. Kwon, H. S. Kim, J. Jeon, Y.-H. Kim, J.-A. Lim, B.-S. Kim, J. Choi, H. Kim, *ACS Catal.* **2018**, *8*, 2420.
- [59] M.-Y. Lee, S. Ringe, H. Kim, S. Kang, Y. Kwon, *ACS Energy Lett.* **2020**, *5*, 2987.